Neural progenitor cell pyroptosis contributes to Zika virus-induced brain atrophy and represents a therapeutic target

Zhenjian He[a,b,1] , Shu An[b,c,1], Jiahui Chen[d,e], Shuqing Zhang[b,c], Chahui Tan[b,c], Jianchen Yu[b,c], Hengming Ye[a,b], Yun Wu[b,c], Jie Yuan[b,e,f], Jueheng Wu[b,c], Xun Zhu[b,c,2], and Mengfeng Li[b,c,g,2]

[a]School of Public Health, Sun Yat-Sen University, 510080 Guangzhou, China; [b]Key Laboratory of Tropical Disease Control (Sun Yat-Sen University), Ministry of Education, 510080 Guangzhou, China; [c]Department of Microbiology, Zhongshan School of Medicine, Sun Yat-Sen University, 510080 Guangzhou, China; [d]Microbiome Medicine Center, Division of Laboratory Medicine, Zhujiang Hospital, Southern Medical University, 510282 Guangzhou, Guangdong, China; [e]Innovation Platform for Public Health of Guangdong Province, Zhujiang Hospital, Southern Medical University, 510282 Guangzhou, Guangdong, China; [f]Department of Biochemistry, Zhongshan School of Medicine, Sun Yat-Sen University, Guangzhou 510080, China; and [g]Cancer Institute, Southern Medical University, 510515 Guangzhou, China

Mounting evidence has associated Zika virus (ZIKV) infection with congenital malformations, including microcephaly, which raises global alarm. Nonetheless, mechanisms by which ZIKV disrupts neurogenesis and causes microcephaly are far from being understood. In this study, we discovered direct effects of ZIKV on neural progenitor cell development by inducing caspase-1– and gasdermin D (GSDMD)-mediated pyroptotic cell death, linking ZIKV infection with the development of microcephaly. Importantly, caspase-1 depletion or its inhibitor VX-765 treatment reduced ZIKV-induced inflammatory responses and pyroptosis, and substantially attenuated neuropathology and brain atrophy in vivo. Collectively, our data identify caspase-1– and GSDMD-mediated pyroptosis in neural progenitor cells as a previously unrecognized mechanism for ZIKV-related pathological effects during neural development, and also provide treatment options for ZIKV-associated diseases.

Zika virus | microcephaly | neurogenesis | pyroptosis | caspase-1

The recent outbreak of Zika virus (ZIKV) epidemics in the Americas has drawn global attention, largely due to its association with the dramatic increase of neonatal microcephaly, in addition to other clinical manifestations similar to those caused by infection of the *Flavivirus* genus. ZIKV belongs to the family *Flaviviridae* (genus *Flavivirus*) and is transmitted through the *Aedes* species mosquitoes or sexually (1, 2). To date, ZIKV has spread rapidly around the world in 87 countries and territories after its initial origination from an outbreak in Brazil (3). Clinical illness caused by ZIKV infection is generally mild and characterized by acute febrile illness associated with rash, arthralgia, and conjunctivitis (4). However, accumulating evidence suggests that ZIKV infection during pregnancy can cause the fetus to be born with microcephaly accompanied with or without other congenital malformations (5–9). A recent report based on analysis of over 4 million births in Brazil during 2015 to 2017 highlighted an association between congenital ZIKV infection and microcephaly, and found an approximate 15- to 75-fold increase in microcephaly risk by ZIKV infection in pregnancy (10). Thus far, 31 countries have reported microcephaly or neurological malformations associated with ZIKV (11).

Microcephaly is a condition in which an infant is born with an abnormally small head or the head stops growing after birth. In more severe cases, growth restriction affects the brain and central nervous system, which may lead to epilepsy, cerebral palsy, learning disabilities, hearing loss, and vision problems (12–14). Evidence supporting an etiological role of ZIKV in microcephaly includes detection of ZIKV in the placenta and amniotic fluid of microcephalic fetuses and in the blood of microcephalic newborns (15–17). Moreover, ZIKV had also been found in the fetal brain tissues from infants with microcephaly (5, 17). Recently, several in vivo and in vitro studies have indicated that ZIKV is

able to infect neural progenitor cells (NPCs), impair the cell cycle, and cause cell death (18–21). Nevertheless, while efforts have been paid to study the mechanism by which ZIKV disrupts neurogenesis and causes microcephaly, it is not fully elucidated, and clinically applicable therapeutic targets are yet to be identified.

Previous studies reported that apoptosis occurred in cells infected by ZIKV (18–21). Examination of ZIKV-infected NPCs and 3D brain organoids showed that ZIKV infection triggered caspase-3–mediated apoptosis, resulting in diminished cortical layers (22). Notably, as a form of programmed cell death to remove unwanted cells, apoptosis represents a process that does not induce inflammatory response (23). Nevertheless, it has been found that high levels of multiple inflammatory cytokines and necrosis can be present in the brains of microcephalic newborns infected by ZIKV, suggesting that ZIKV may also cause other forms of cell death (17, 24). A recent study performed in brain tissue samples of ZIKV⁺ microcephaly cases has revealed an activation of inflammasome-associated genes, indicating that activation of inflammasome and pyroptosis may aggravate neuroinflammation and consequently

> ## Significance
>
> Zika virus (ZIKV) has been identified as a cause of microcephaly. However, the mechanisms by which ZIKV disrupts neurogenesis and causes microcephaly remains poorly understood. Here, we first report that ZIKV exposure causes neural progenitor cell pyroptosis, mediated by activation of caspase-1 and gasdermin D in vivo as well as in vitro, which links ZIKV to the development and progression of microcephaly. Consistent with this notion, caspase-1 deletion or treatment with caspase-1 inhibitor VX-765 reduced ZIKV-induced inflammatory responses and pyroptosis, and robustly attenuated neuropathy and brain atrophy. Taken together, our findings provide unique perspectives on ZIKV-associated neuropathogenesis and potentially clinically applicable options for its treatment.

increase central nervous system damage in neonates with ZIKV-associated microcephaly (25). In addition, several studies performed in mice further demonstrated that the nucleotide and oligomerization domain, leucine-rich repeat-containing protein family, pyrin-containing domain 3 (NLRP3) inflammasome activation could mediate ZIKV-associated neuroinflammation and suggested that pyroptosis may also contribute to the neuropathogenesis of ZIKV infection (26, 27). In such a context, pyroptosis has been identified as a highly inflammation-associated programmed cell death, characterized by pore formation on the plasma membrane, cell swelling, and plasma membrane disruption and consequent releases of their cytoplasmic contents, including inflammatory cytokines, into the extracellular environment (28). Pyroptosis can be initiated by microbial products or endogenous stimuli that stimulate pattern recognition receptors (PRRs), resulting in the formation of the inflammasome, a multiprotein complex consisting of a PRR as the sensor, the adaptor apoptosis-associated speck-like protein containing a caspase-recruitment domain (ASC), and the cysteine protease caspase-1 (29, 30). The inflammasome subsequently coordinates cleavage and activation of caspase-1. Caspase-1 was first recognized as a protease that cleaves the inactive precursors of IL-1β and IL-18 into mature inflammatory cytokines. Furthermore, activated caspase-1 cleaves the pore-forming protein, gasdermin D (GSDMD), ultimately resulting in releasing its N-terminal fragment, termed gasdermin N, to bind membrane lipids and form pores, leading to cell swelling with large bubbles extruding from the plasma membrane (31–33).

It is noteworthy that pyroptosis involves cell lysis, causes a massive release of cellular contents, and thereby triggers robust inflammation, contributing to the development of many autoimmune and inflammatory diseases (34). Recent studies have shown that pyroptosis can be a primary cause of such diseases as anthrax-lethaltoxin–induced lung injury and hematopoietic progenitor cell depletion in mice (35, 36). Moreover, pyroptosis mediated by caspase-1 in HIV infection accounts for CD4$^+$ T cell depletion, a critical event in HIV pathogenesis (37). Our previous studies have revealed that ZIKV activates NLRP3 inflammasomes in mice, indicating that pyroptosis might be involved in the pathogenesis of ZIKV infection (26). Whether pyroptosis participates in ZIKV-induced cell death of neural cells in the brain and leads to neuropathology and microcephaly, however, has not been studied.

In this study, our data show that neonatal ZIKV infection in mice causes severe brain inflammation, neuro-tissue damage, and postnatal-onset brain atrophy. We reveal that ZIKV exposure causes pyroptosis in neural cells, including NPCs, astrocytes, and microglia, mediated by activation of caspase-1 and GSDMD in vivo as well as in vitro, which experimentally links ZIKV with the development and progression of microcephaly. It is of great interest that our results demonstrate that caspase-1 deletion or treatment with caspase-1 inhibitor VX-765, which underwent phase I and II clinical trials for other diseases, reduced ZIKV-induced inflammatory responses and pyroptosis, and robustly attenuated neuropathy and brain atrophy. Together, our findings provide unique perspectives on ZIKV-associated neuropathogenesis and potentially clinically applicable options for its treatment.

Results

ZIKV Replicates in Neonatal Mouse Brain and Causes Severe Neuropathological Alterations and Brain Atrophy.
To evaluate whether ZIKV infection is pathogenic during brain development in mice, WT mouse pups of immunocompetent mice at postnatal day 3 (P3), a time point when the development of rodent brain and immune system resembles the second and third trimesters of gestation in humans (38, 39), were subcutaneously mock-infected or infected with 5×10^5 plaque formation units (PFUs) of ZIKV. Notably, the ZIKV-infected mice displayed lower body weight than the mock-infected mice during the period from 3 d postinfection (dpi) through 21 dpi (Fig. 1A). Furthermore, autopsy

examination found marked brain atrophy in the ZIKV-infected mice, as demonstrated by decreased dorsal brain area at 21 dpi (Fig. 1 B and C). Using a qRT-PCR assay, high numbers of viral RNA copies were confirmed to be present in the brains of ZIKV-infected mice, suggesting that the observed brain atrophy was closely associated with the ZIKV infection (Fig. 1D). To further investigate the possible pathogenic effect of ZIKV infection on brain development, tissue sections of the murine brains were subject to neuropathological examination. Of note, the ZIKV-infected mouse brains showed massive neutrophilic infiltration, necrosis, and disruption of the normal cytoarchitecture predominantly in the hippocampus, thalamus, and cortex areas, indicating severe focal inflammation in the brain, whereas the mock infection causes no pathological changes (Fig. 1 E and F). Moreover, brains of ZIKV-infected mice showed frequent perivascular cuffs of mononuclear cells and microglial cells (Fig. 1 E and F). Taken together, our findings indicate that ZIKV infection causes brain atrophy and induces robust inflammatory brain damages in the murine infection model employed.

ZIKV Infection Causes NPC Pyroptosis In Vivo.
In light of previous studies having shown tropism of ZIKV to NPCs and caspase-3–mediated apoptotic cell death (18, 19), based on our aforementioned observation of inflammatory damages in the ZIKV-infected mouse brains, we further asked whether ZIKV infection can also trigger caspase-1–mediated pyroptosis in NPC populations in the brain. When stained for cleaved caspase-1 (p10) and propidium iodide (PI) in NPC niches with indicated markers, as shown in Fig. 2 A and B, mock-infected mice brains showed scant evidence of caspase-1$^+$ and PI$^+$ cells, while in contrast ZIKV-infected mice exhibited abundant cleaved caspase-1 and PI$^+$ cells within these neurogenic niches. Other cells types, such as neurons, astrocytes, and microglia were also investigated and stained for cleaved caspase-1 (p10) with cell type-specific markers. As shown in *SI Appendix*, Fig. S1, cleaved caspase-1 (p10) reactivity was detected in a small number of NeuN-expressing neurons and glial fibrillary acidic protein (GFAP)-expressing astrocytes, but not in ionized calcium-binding adapter molecule 1 (Iba-1)–expressing microglia, suggesting that ZIKV infection might indeed induces pyroptotic cell death in various types of cells in the brain.

As pyroptosis is mechanistically connected to inflammasome activation, a wider panel of inflammasome genes was next assessed in the brain tissue specimens obtained from the ZIKV-infected and the mock-infected mice. As shown in Fig. 2C, all inflammasome-associated genes were detectable in the mouse brain tissue specimens, with levels of *IL1B, IL-18, CASP1, ASC,* and *GSDMD* transcripts being remarkably elevated in those derived ZIKV-infected mice, as compared with the mock infection. Moreover, while inflammasome sensor genes, including *MEFV* (coding for pyrin), *NLRP1, NLRP2, NLRP3,* and *AIM2* were also detectable in all mouse brain tissues, *NLRP3* expression increased most significantly in ZIKV-infected brains when compared with the mock controls (Fig. 2D). In addition, as cleavage and formation of activated N-terminal domain of GSDMD (GSDMD-N) by activated caspase-1 was recently identified as an executioner of pyroptosis (31, 32), we next examined whether ZIKV infection could induce proteolytic cleavage of GSDMD. Our results showed that significant degrees of both caspase-1 and GSDMD cleavages indeed occurred in the ZIKV-infected brains (Fig. 2E). Taken together, these data support the notion that ZIKV infects NPCs and triggers pyroptotic cell death in vivo.

ZIKV Infects Human NPCs and Induces Pyroptosis In Vitro.
To further understand the possible connection between ZIKV and impairment of neurogenesis, we next evaluated the biological effect of ZIKV-induced pyroptosis on cultured human NPCs (hNPCs). hNPCs were first exposed to ZIKV at a multiplicity of infection
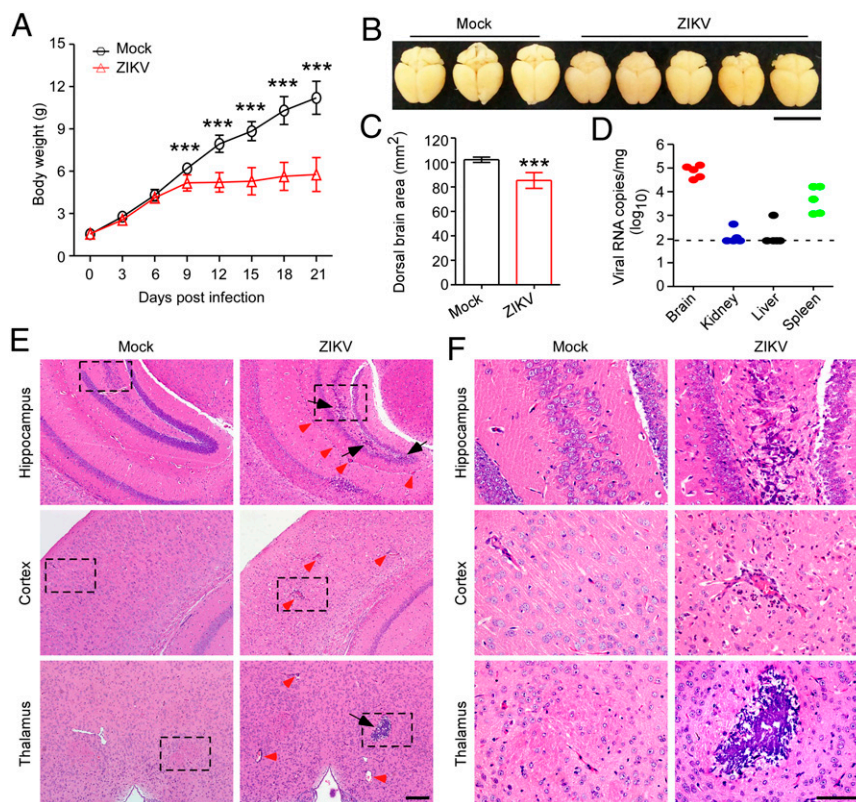
Fig. 1. ZIKV infection leads to severe neuropathological alterations and brain atrophy in mice. Three-day-old mouse pups of immunocompetent mice were subcutaneously injected with 5×10^5 PFUs of ZIKV, or were mock-infected. (*A*) Body weight curves of mock- and ZIKV-infected mice ($n = 12$). (*B*) Representative images of brains obtained from mock- and ZIKV-infected mice (21 dpi). (Scale bar, 1 cm.) (*C*) Quantification of dorsal brain area is shown in the histogram ($n = 10$). (*D*) ZIKV RNA in mice specimens was quantified by qRT-PCR (21 dpi) ($n = 5$). Dotted line depicts the limit of detection for the assays. (*E*) Representative micrographs of histopathological analysis with H&E staining of brain sections (21 dpi). Black arrows: necrotic loci; red arrowheads: perivascular cuffing. (Scale bar, 100 μm.) (*F*) Representative micrographs of the hippocampus, cortex, and thalamus of ZIKV- and mock-infected mice brain (21 dpi). (Scale bar, 50 μm.) All data are presented as mean ± SD, Student's *t* test, ***$P < 0.001$.

(MOI) of 1 for 36 h and morphological examination found typical pyroptotic changes with cell swelling and membrane rupture being identified in ZIKV-infected hNPCs, but not in the mock controls (Fig. 3*A*). ZIKV infection in hNPCs was verified by costaining of ZIKV E antigen and SOX2 in cells (Fig. 3*B*). In addition, ultrastructural analysis by transmission electron microscopy (TEM) also revealed necrotic morphological changes showing clumps of chromatin, swollen mitochondria, and disruption of plasma membrane following ZIKV infection (Fig. 3*C*). We next examined the activity of caspase-1 in the cell lysates, and the data showed increased caspase-1 activity in cells infected by ZIKV (Fig. 3*D*). Moreover, pyroptotic cells were further verified by PI/Hoechst 33342 double-staining assay, and as expected, hNPCs infected with ZIKV underwent pyroptosis (Fig. 3 *E* and *F*). To quantify the loss of membrane integrity during pyroptosis, lactate dehydrogenase (LDH) activity was measured in cell culture supernatants, indicating extravasation of cellular contents. As Fig. 3*G* shows, the amount of LDH release markedly increased by ZIKV infection as compared to mock infection, whereas silencing caspase-1 expression reduced the amount of LDH release caused by ZIKV infection as compared to the siRNA negative control, suggesting that caspase-1–mediated pyroptosis in NPCs, contributes to ZIKV pathogenesis. Furthermore, ZIKV infection triggered cleavage of caspase-1 and GSDMD in hNPCs, when compared with the mock-infected counterpart cells (Fig. 3*H*). In these experiments, nigericin, which promotes NLRP3 inflammasome assembly, caspase-1 activation, and pyroptosis, was used as a positive control (40). Together, the above findings further demonstrate the caspase-1–mediated propyroptotic- and pytoptosis-associated effects of ZIKV infection in hNPCs culture model.

ZIKV Induces Pyroptotic Cell Death in Human Neurospheres. To further illustrate the biological effects of ZIKV infection during neurogenesis, we next infected 3D culture of neural cells with ZIKV and then observed formation of neurospheres using a previously established method (20). We found that mock-infected hNPCs generated round neurospheres, whereas ZIKV-infected neurospheres exhibited morphological abnormalities with signs of pyroptotic cell death (Fig. 4 *A* and *B*). Moreover, the mock-infected neurospheres continued to grow over time, but only a few ZIKV-infected neurospheres survived with smaller sizes (Fig. 4 *A–D*). To further validate that the neurospheres infected with ZIKV underwent pyroptosis, we double-stained neurospheres with active caspase-1 and PI. As shown in Fig. 4*E*, neurospheres infected with ZIKV contained intensely stained active caspase-1 and PI, indicating that ZIKV infection can induce pyroptosis in neurospheres. In these experiments, neurospheres infected with ZIKV was verified by costaining of ZIKV E antigen and SOX2 in the neurospheres (Fig. 4*F*), and furthermore, LDH release from neurospheres following ZIKV infection was also determined, showing that ZIKV infection induced LDH release from neurospheres (Fig. 4*G*). Collectively, these findings further confirmed the capability of ZIKV to induce neurospheres pyroptosis and impaired the growth and morphogenesis of healthy neurospheres.

Depletion of Caspase-1 Reverses ZIKV-Induced Neuropathological Alterations and Brain Atrophy. Based on our findings that caspase-1–mediated pyroptosis could be triggered by ZIKV infection in NPCs and neurospheres in the brain, we next generated *caspase-1*–null
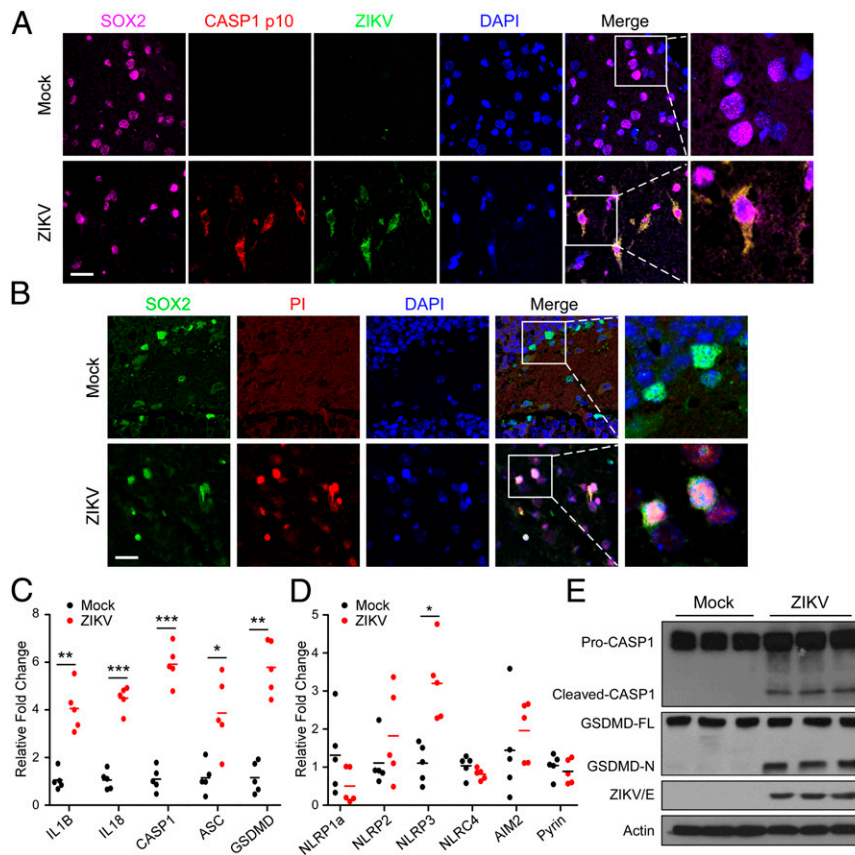
Fig. 2. ZIKV infection induces NPCs pyroptosis in vivo. (*A*) Representative micrographs of the brain tissue costained for SOX2, cleaved caspase-1 (p10), and ZIKV NS3 protein (21 dpi). The nuclei were stained with DAPI. (Scale bar, 25 μm.) (*B*) Representative micrographs of the brain tissue costained for SOX2 and PI (21 dpi). The nuclei were stained with DAPI. (Scale bar, 25 μm.) (*C* and *D*) Relative expression levels of inflammasome-associated genes were determined using qRT-PCR in mice brain specimens (21 dpi) ($n = 5$). (*E*) Examination of the proteolytic cleavage of caspase-1 and GSDMD in mice brain specimens with ZIKV- or mock- infection, using immunoblotting analysis (21 dpi). GSDMD-FL, full-length GSDMD; GSDMD-N, the N-terminal cleavage product of GSDMD. All data are presented as mean ± SD, Student's *t* test, *$P < 0.05$, **$P < 0.01$, ***$P < 0.001$.

background mice to further evaluate the role of pyroptosis in the pathogenesis of ZIKV-induced brain malformation in vivo. Specifically, after 3-d-old mouse pups of WT or *caspase-1*–deficient ($Casp1^{-/-}$) were subcutaneously infected with 5×10^5 PFUs of ZIKV or mock-infected, we found that WT mice infected with ZIKV exhibited lower body weight as compared with mock-infected groups, whereas the body weights of ZIKV-infected $Casp1^{-/-}$ mice were similar to those of the mock-infected groups at 21 d (Fig. 5*A*). Compared with the ZIKV-infected WT mice, severe brain atrophy was drastically abrogated in the $Casp1^{-/-}$ mice infected by ZIKV (Fig. 5 *B* and *C*). Histopathological examination further indicated that $Casp1^{-/-}$ mice were all spared from inflammation-induced damage, in contrast to the ZIKV-infected WT mice (Fig. 5*D* and *SI Appendix*, Fig. S2). Moreover, when the expression levels of proinflammatory cytokines IL-1β and IL-18 were measured in brain tissues, we found that depletion of caspase-1 abolished the increase of IL-1β and IL-18 in mice infected with ZIKV, as compared with those in their WT counterparts (Fig. 5 *E* and *F*). In addition, our results showed that ZIKV infection triggered a cleavage of GSDMD, while caspase-1 ablation attenuated GSDMD cleavage, as assessed by immunoblotting analysis, indicating inhibition of pyroptosis in the brains of these mice (Fig. 5*G*). Accordingly, neuropathology and brain atrophy caused by ZIKV could be restrained by abrogation of caspase-1–mediated pyroptosis.

VX-765 Treatment Alleviates Neuropathology and Brain Atrophy in ZIKV-Infected Mice. The important role of caspase-1 in mediating ZIKV-associated neuropathology prompted us to investigate whether

caspase-1 can be a potential therapeutic target for neuropathology and microcephaly. VX-765, a prodrug of VRT-043198, is a potent and selective inhibitor of caspase-1 with an ability to permeate the blood–brain barrier and is pharmacologically well tolerated (41, 42). In our attempt to further determine whether VX-765 was able to influence ZIKV-associated neuropathological outcome in vivo, we treated 3-d-old mouse pups subcutaneously infected with 1×10^6 PFUs of ZIKV or mock-infected with VX-765 (50 mg/kg, i.p.), using caspase-3 inhibitor Z-DEVD-FMK (50 mg/kg, i.p.) and carrier solvent (PBS/DMSO) as controls. Our results showed that mice treated with control vehicle or Z-DEVD-FMK gained weight slower than the mock-infected control mice, whereas this consequence did not occur in mice treated with VX-765 (Fig. 6*A*). Thirty days later, the survival rate of ZIKV-infected mice was only 38%, and in contrast, mice treated with VX-765 displayed a higher survival rate of 69%. Whereas all mice treated with Z-DEVD-FMK died by day 16 after infection (Fig. 6*B*), further observation showed no significant difference in body weight changes and survival between mice treated with Z-DEVD-FMK and those with vehicle or VX-765 without ZIKV infection, suggesting that caspase-3 inhibition increased, rather than alleviated the lethality of mice infected by ZIKV (*SI Appendix*, Fig. S3 *A* and *B*). Furthermore, as compared with the vehicle control-treated ZIKV-infected mice, severe brain atrophy caused by ZIKV infection was attenuated by VX-765 treatment (Fig. 6 *C* and *D*). Brain sizes of mice treated with VX-765 or Z-DEVD-FMK without ZIKV infection showed no difference when compared to mock infection of vehicle control treatment (*SI Appendix*, Fig. S3 *C* and *D*).
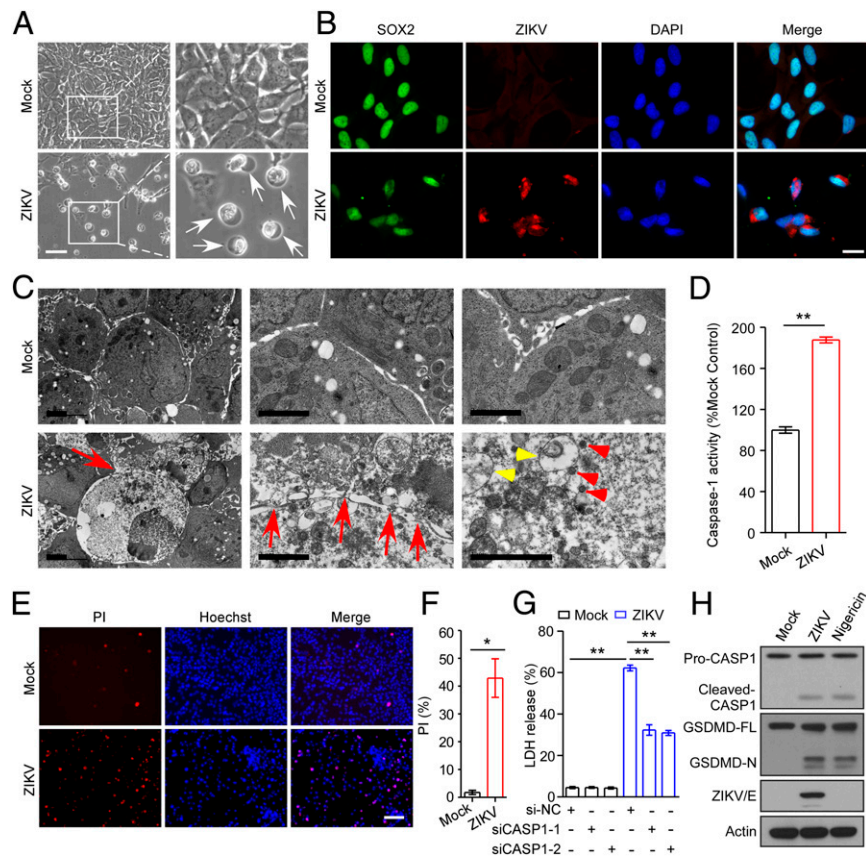
Fig. 3. ZIKV infects cultured hNPCs and induces pyroptosis. (*A*) Phase-contrast cell images of hNPCs with ZIKV or mock infection (white arrows, pyroptotic cells). (Scale bar, 50 μm.) (*B*) Representative micrographs of hNPCs double-stained for ZIKV (E protein) and SOX2 at 36 hpi (MOI = 1). The nuclei were stained with DAPI. (Scale bar, 400 μm.) (*C*) Representative transmission electron micrographs of mock- and ZIKV-infected hNPCs. Red arrows: membrane pores, Yellow arrowheads: mitochondria with collapsed cristae; red arrowheads: immature viral particles. (Scale bars, 2 μm.) (*D*) Caspase-1 activity was determined in cell lysates from mock- and ZIKV-infected hNPCs. (*E*) Representative micrographs of PI and Hoechst 33342 staining of hNPCs with ZIKV or mock infection. Red: PI dye; blue: Hoechst 33342 dye. (Scale bar, 100 μm.) (*F*) Quantification of the number of PI$^+$ cells relative to mock infection is shown in the histogram. (*G*) LDH release was measured in supernatant derived from mock- and ZIKV-infected hNPCs transfected with small-interfering RNAs (siRNAs) targeting caspase 1. (*H*) Proteolytic cleavage of caspase-1 and GSDMD in hNPCs with ZIKV or mock infection was examined by immunoblotting analysis. Nigericin induced abundant caspase-1 and GSDMD activation in uninfected cells served as a positive control. GSDMD-FL, full-length GSDMD; GSDMD-N, the N-terminal cleavage product of GSDMD. All data are presented as mean ± SD, Student's *t* test, *$P < 0.05$, **$P < 0.01$.

Further histopathological examination showed that massive neutrophilic infiltration and necrotic loci was observed in the hippocampus of ZIKV-infected control and Z-DEVD-FMK–treated mice but was potently attenuated after the VX-765 treatment (Fig. 6*E*). No apparent neuroinflammation was observed in mice treated with control vehicle, VX-765, or Z-DEVD-FMK without ZIKV infection (*SI Appendix,* Fig. S3*E*). Immunohistochemistry (IHC) analysis for Iba-1–, and GFAP-specific markers for microglia and astrocytes, respectively, was used to assess neuroinflammation in the brains. As shown in Fig. 6*F*, both Iba-1 and GFAP levels were significantly higher in the hippocampus of ZIKV-infected control- and Z-DEVD-FMK–treated mice than the mock-infected mice. Of note, VX-765 administration robustly decreased the expression of Iba-1 and GFAP to levels comparable to brains of uninfected mice, suggesting that VX-765 was able to reverse neuroinflammation.

Furthermore, the expression levels of proinflammatory cytokines IL-1β and IL-18 were up-regulated in the brain tissues of control vehicle-treated mice exposed to ZIKV, whereas such an up-regulation was repressed by VX-765 treatment, but not Z-DEVD-FMK (Fig. 6 *G* and *H*). Correspondingly, after VX-765 treatment, proteolytic cleavage of both caspase-1 and GSDMD was found to be inhibited in the brains of ZIKV-infected mice as compared

with that in the vehicle-control or Z-DEVD-FMK–treated counterparts, indicating that VX-765 indeed suppress pyroptosis associated with ZIKV infection in vivo (Fig. 6*I*). It is additionally noteworthy that ZIKV replication in mice was repressed by VX-765, but enhanced by Z-DEVD-FMK (*SI Appendix,* Fig. S4). Together, the above data suggest that inhibition of pyroptosis indeed improve the neuropathological outcome caused by ZIKV infection.

In this study, type-I IFN receptor-deficient (*Ifnar1*$^{-/-}$) mice were also used to generate a ZIKV infection model to further evaluate the effect of VX-765 on reducing neuroinflammation and pyroptosis. Notably, VX-765 treatment improved survival rates of mice infected with ZIKV (*SI Appendix,* Fig. S5*A*). Histopathological examination revealed that while ZIKV infection induced severe inflammatory responses in the brains of mice, such ZIKV-induced inflammatory responses were repressed by VX-765 (*SI Appendix,* Fig. S5*B*). Moreover, VX-765 also inhibited IL-1β and IL-18 production and GSDMD cleavage in the ZIKV-infected mice brains (*SI Appendix,* Fig. S5 *C* and *D*). Taken together, these results demonstrate that VX-765 treatment exerts significant and sustained beneficial effects on ZIKV-associated neuropathy and brain atrophy in conjunction with reduced neuroinflammation and pyroptosis.
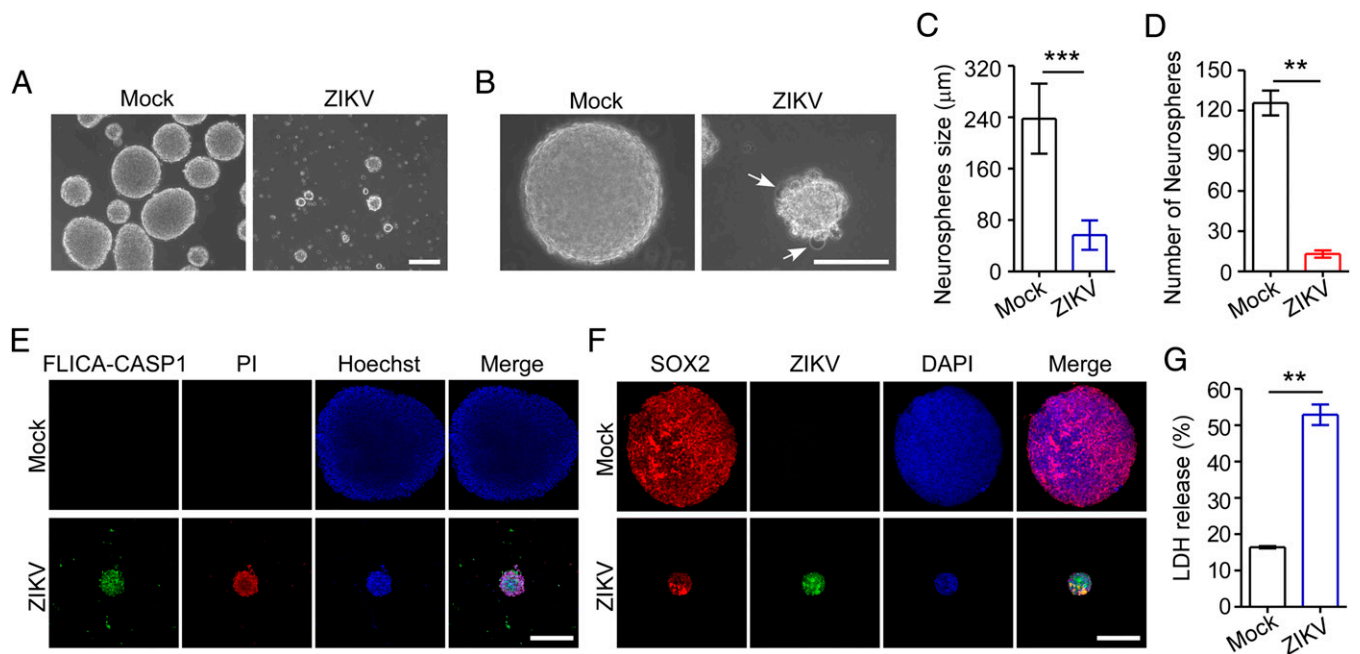
Fig. 4. ZIKV infects human neurospheres and induces pyroptosis. (*A* and *B*) Representative micrographs of human neurospheres infected with ZIKV (MOI = 0.5; 96 hpi) or mock infection. White arrows: pyroptotic cells. (Scale bar, 200 μm in *A* and 100 μm in *B*.) (*C* and *D*) Quantification of the diameter (*C*) and number (*D*) of neurospheres is shown in the histogram. (*E*) Representative micrographs of neurospheres double-stained for active caspses-1 with a FLICA probe conjugated with FAM (green), and PI (red) at 96 hpi (MOI = 0.5). Nuclei were visualized by staining with Hoechst 33342 (blue). (Scale bar, 100 μm.) (*F*) Representative micrographs of neurospheres double-stained for ZIKV (E protein) and SOX2 at 96 hpi (MOI = 0.5). The nuclei were stained with DAPI. (Scale bar, 100 μm.) (*G*) LDH release was measured in supernatant taken from cultured mock- and ZIKV-infected neurospheres. All data are presented as mean ± SD, Student's *t* test, **$P < 0.01$, ***$P < 0.001$.

Discussion

Here we demonstrate that ZIKV infection in neonatal mice displays a tropism for neurogenic niches in the brain and leads to cellular pyroptosis associated with neuropathological alterations and brain atrophy. Importantly, we found that inhibition of pyroptosis by caspase-1 ablation or VX-765 treatment potently attenuates neuropathy and brain atrophy caused by ZIKV infection. These findings reveal a previously unidentified mechanism underlying which ZIKV infection results in microcephaly, and provide a foundation for the potential applicability of antipyroptotic treatment against ZIKV-associated diseases.

Microcephaly is a severe brain malformation characterized by reduction of the head circumference due to abnormal development during pregnancy, or impeded growth of the brain after birth. Neonates with microcephaly show a heterogeneous manifestation of brain impairments involving damaged cognitive, visual, hearing, and motor functions (43). The etiology of microcephaly is heterogeneous, ranging from genetic causes to environmental factors, including genetic disorders, infection of pathogens (e.g., toxoplasma or rubella virus), exposure to toxic chemicals during pregnancy, and severe malnutrition during fetal life (44). After the outbreak of ZIKV in Brazil, substantial evidence indicates a causal link between ZIKV and microcephaly (5–9). In this study, we evaluated the pathogenic effects of ZIKV infection on brain malformation during development by infecting mouse pups of normal, immune-competent mice at P3, a period of rodent brain and immune system development that resembles the second and third trimesters of human fetus (38, 39). In agreement with previous studies (45, 46), we found that mice subjected to early-life infection by ZIKV display neuropathological alterations and brain atrophy after infection, and that ZIKV triggers neural cells, including NPCs, astrocytes, and microglia cell death in the brain. Interestingly, while several previous studies suggested the presence of apoptosis, a noninflammatory form of programmed cell death to

remove unwanted cells (23), in ZIKV-infected cells (18–21), our present data reveal high levels of multiple inflammatory cytokines and necrosis in the brains of newborns infected with ZIKV, strongly suggesting that ZIKV infection also causes other forms of cell death associated with inflammatory responses (17, 24). In this context, our present data reveal that neural cells indeed undergo pyroptosis following ZIKV infection in vitro and in a brain atrophy mouse model in vivo. In conjunction with our further evidence that pyroptosis, but not apoptosis inhibition, is therapeutic for ZIKV-induced brain atrophy, we here propose a previously unrecognized, pyroptosis-based neuropathogenic mechanism that directly links ZIKV infection to the pathogenesis of microcephaly during neural development.

Pyroptosis represents a highly inflammatory form of programmed cell death distinct from apoptosis or other types of cell death. In contrast to apoptosis, pyroptosis is triggered by caspase-1 after its activation by various inflammasomes and results in cellular lysis and early release of the cytosolic contents to the extracellular space, including proinflammatory cytokines (47). Activation of pyroptosis promotes rapid clearance of infection of various bacteria and viruses by removing intracellular replication niches and enhancing host defense response through the release of proinflammatory cytokines (28). The biological effects of pyroptosis, however, can also be deleterious, as the resultant pyroptotic cell death and increased inflammatory cytokines play important roles in the pathogenesis of inflammatory diseases (34). For example, pyroptosis has been shown to be a primary cause of anthrax-lethaltoxin–induced lung injury and hematopoietic progenitor cell depletion (35, 36). In addition, pyroptosis mediated by caspase-1 in HIV infection accounts for CD4+ T cell depletion, a critical event in HIV pathogenesis (37). Here, we show that ZIKV infection triggers pyroptosis in NPCs and disrupts formation of neurospheres, leading to impairment of neurogenesis. In such a context, our study facilitates understanding how ZIKV causes microcephaly and developing of antipyroptotic therapies and provides a rationale
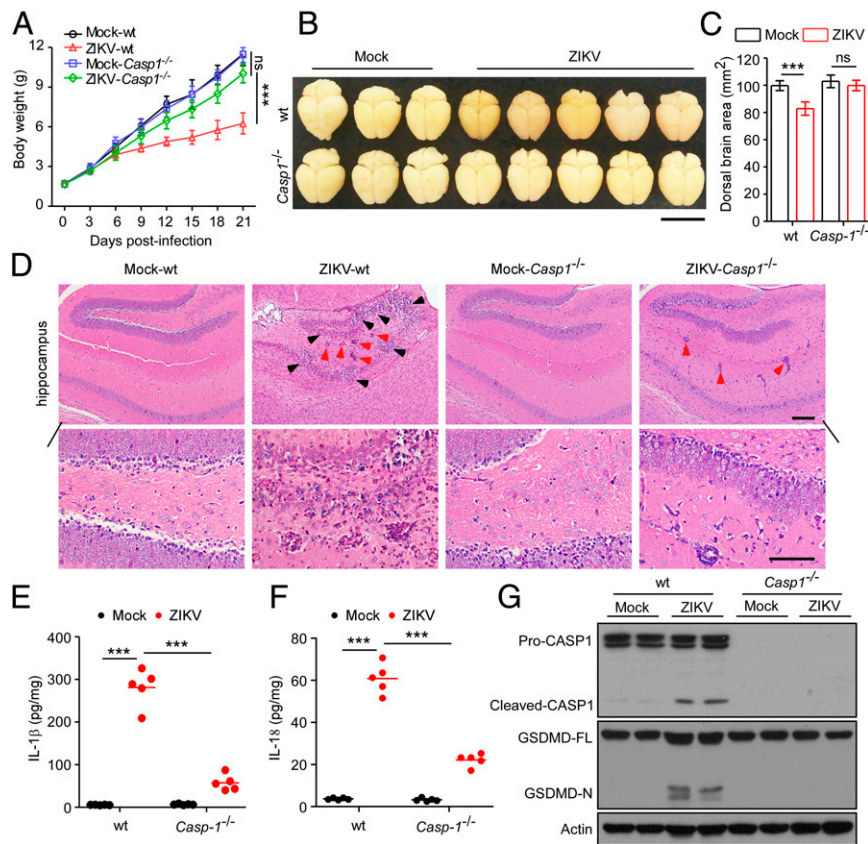
Fig. 5. *Caspase-1* KO restores neuropathological alterations and brain atrophy induced by ZIKV in mice. Three-day-old mouse pups of WT or *Casp1*$^{-/-}$ were subcutaneously infected with 5×10^5 PFUs of ZIKV or mock-infected. (*A*) Body weight curves of WT or *Casp1*$^{-/-}$ mice with ZIKV and mock infection ($n = 10$). (*B*) Representative images of brains taken from WT or *Casp1*$^{-/-}$ mice infected with ZIKV or mock infection (21 dpi). (Scale bar, 1 cm.) (*C*) Dorsal brain area was analyzed and shown in the histogram (21 dpi) ($n = 10$). (*D*) Representative micrographs of the hippocampus of WT or *Casp1*$^{-/-}$ mice (21 dpi). (Scale bars, 100 μm [*Upper*], 50 μm [*Lower*].) Black arrowheads: necrotic loci; red arrowheads: perivascular cuffing. (*E* and *F*) IL-1β and IL-18 were measured with ELISA in brain samples of WT and *Casp1*$^{-/-}$ mice with ZIKV and mock infection (21 dpi). (*G*) Proteolytic cleavage of caspase-1 and GSDMD in brain specimens of WT and *Casp1*$^{-/-}$ mice with ZIKV- and mock-infection was determined by immunoblotting analysis (21 dpi). GSDMD-FL, full-length GSDMD; GSDMD-N, the N-terminal cleavage product of GSDMD. All data are presented as mean ± SD, Student's *t* test, **$P < 0.01$, ***$P < 0.001$. ns, not significant.

for future pyroptosis-targeted interventional strategies for severe ZIKV diseases.

Notably, recent advances in understanding the key role of pyroptosis in the pathogenesis of inflammatory diseases have provided novel targets, such as caspase-1, for new therapeutic strategies against an expanding number of inflammatory diseases. VX-765, a prodrug of VRT-043198, is a potent and selective inhibitor of caspase-1, which is able to permeate the blood–brain barrier and pharmacologically well tolerated, has been shown to suppress IL-1β and IL-18 release in oxalozone-induced murine dermatitis and rheumatoid arthritis models (41, 42, 48). Additional data demonstrate that VX-765 prevents CD4$^+$ T-cell pyroptotic death in a dose-dependent manner in HIV-infected lymphoid tissues (37). In the present study, a variety of in vitro and in vivo experiments were performed to determine the effect of VX-765 on ZIKV-associated outcomes, and our data revealed that VX-765 treatment effectively alleviates ZIKV-induced neuropathy and brain atrophy in the neonatal mouse model. Moreover, to generate an additional, independent ZIKV infection model to further evaluate the therapeutic effect of VX-765, *Ifnar1*$^{-/-}$ mice were also employed, in which we found that VX-765 treatment reduced the severity of inflammatory responses in the brains of mice and improved survival rates of mice infected by ZIKV. Of note, VX-765 has been proved to be safe and well tolerated in phase 2b human trials against epilepsy (49). Brain penetrance data performed in mouse models have also verified that VX-765 can

cross the blood–brain barrier (41, 42). Moreover, previous study using in vitro chorioamniotic membrane models have reported that VX765 inhibited LPS-induced release of inflammasome-dependent IL-1β and IL-18 by the chorioamniotic membranes, indicating that VX765 may cross chorioamniotic membranes or the placental barrier to implement its effect (50). Therefore, VX-765 may represent a safe drug that could easily and rapidly be clinically tested for its efficacy against ZIKV-associated inflammatory diseases, including microcephaly. Taken together, our data, and others', suggest that it may be worthwhile testing the capability of the drug to cross the placental barrier, as fetal inflammatory diseases caused by mother-to-child transmission of ZIKV remains a serious threat to both maternal and fetal health.

In the present study, Z-DEVD-FMK was used to test the effect of blocking caspase-3–mediated apoptosis on brain atrophy in comparison with the therapeutic effect of VX-765. Our results showed that severe brain atrophy and neuroinflammation caused by ZIKV infection could be attenuated by VX-765 treatment, but not by Z-DEVD-FMK. Further investigation found that ZIKV replication in mice was repressed by VX-765, but somewhat enhanced by Z-DEVD-FMK. The above findings indicated that inhibition of apoptosis by targeting caspase-3 seemed to aggravate ZIKV replication and disease in our model. As a form of programmed cell death to remove unwanted cells, apoptosis has been reported to be a host strategy to limit virus replication in certain contexts (51). Of note, such a notion is also echoed by the previous
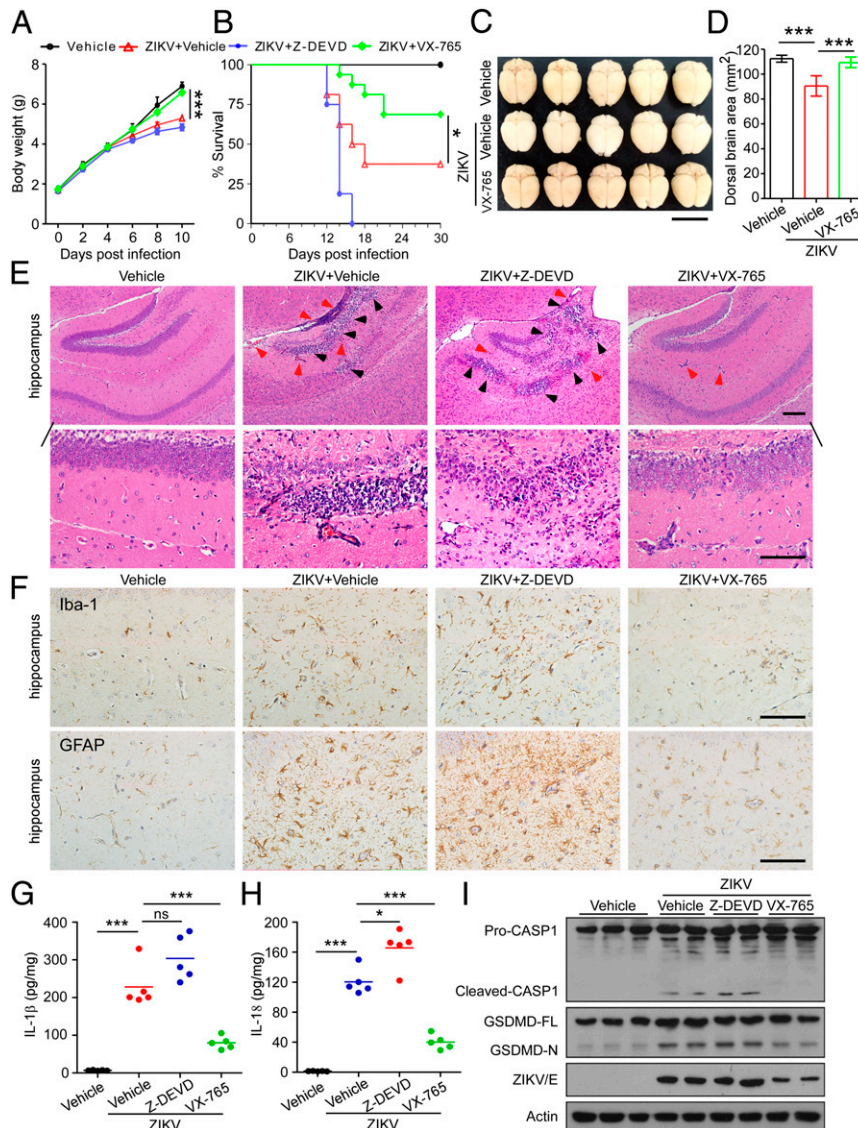
Fig. 6. VX-765 alleviates neuroinflammation and brain atrophy in ZIKV-infected mice. Three-day-old mouse pups were subcutaneously infected with 1×10^6 PFUs of ZIKV- or mock-infected, and subsequently treated with VX-765 (50 mg/kg, i.p.), or Z-DEVD-FMK (50 mg/kg, i.p.), or with vehicle (PBS/DMSO) every 2 d. (*A*) Body weight curves of ZIKV- and mock-infected mice treated with VX-765, Z-DEVD-FMK, or control vehicle (*n* = 16). (*B*) Survival curves of ZIKV- and mock-infected mice treated with VX-765, Z-DEVD-FMK, or control vehicle (*n* = 16). (*C*) Representative images of brains from mock- and ZIKV-infected mice treated with VX-765 or vehicle (30 dpi). (Scale bar, 1 cm.) (*D*) Dorsal brain area of mice was measured and shown in the histogram (*n* = 10). (*E*) Representative micrographs of histopathological analysis with H&E staining of the hippocampus of ZIKV- and mock-infected mice treated with VX-765, Z-DEVD-FMK, or vehicle (30 dpi). (Scale bars, 100 μm [*Upper*], 50 μm [*Lower*].) Black arrowheads: necrotic loci; red arrowheads: perivascular cuffing. (*F*) Representative micrographs of immunohistochemistry of brain sections stained for Iba-1 and GFAP (30 dpi). (Scale bars, 50 μm.) (*G* and *H*) IL-1β and IL-18 were measured with ELISA in brain specimens of ZIKV- and mock-infected mice treated with VX-765, Z-DEVD-FMK or vehicle (30 dpi). (*I*) Proteolytic cleavage of caspase-1 and GSDMD in brain specimens of indicated mice was determined by immunoblotting analysis (30 dpi). GSDMD-FL, full-length GSDMD; GSDMD-N, the N-terminal cleavage product of GSDMD. All data are presented as mean ± SD, Student's *t* test, *$P < 0.05$, **$P < 0.01$, ***$P < 0.001$.

finding that viruses encode protein inhibitors that prevent or delay host cell death so that virus replication can continue. For example, Skaletskaya et al. (52) reported that vICA of human cytomegalovirus could inhibit Fas-mediated apoptosis and facilitate viral infection. In addition, Zhirnov et al. (53) demonstrated that the NS1 protein of influenza A viruses has IFN-dependent antiapoptotic potential, further underscoring the complex roles of apoptosis in the host–virus interplay. Nevertheless, whether and in what context apoptosis impedes ZIKV infection in murine brains, and thereby an apoptosis inhibitor, would enhance ZIKV pathogenesis needs further investigation.

In summary, our findings identify caspase-1–mediated pyroptosis in neural cells, a formerly unknown mechanism for the ZIKV-related pathological effects during neural development, and also provide treatment options for ZIKV-associated diseases.

Materials and Methods

Cell Culture and Virus. The ReNcell VM hNPCs (EMD Millipore) were cultured as previously described (54). Cells were plated on laminin-coated T-25 cell culture flasks and maintained at 37 °C with 5% CO_2 in ReNcell Maintenance Medium supplemented with 20 ng/mL fibroblast growth factor 2 and 20 ng/mL epidermal growth factor (EMD Millipore). Vero cells (obtained from the Cell Bank of the Chinese Academy of Sciences, Shanghai, China) were maintained at 37 °C with 5% CO_2 in DMEM supplemented with 10% FBS (Gibco), 2 mM L-glutamine, 100 μg/mL streptomycin, and 100 U/mL penicillin. *Aedes albopictus* mosquito cells (C6/36) (ATCC CRL-1660) were maintained at 28 °C with 5% CO_2 in DMEM supplemented with 10% FBS. All cell lines were

tested negative for mycoplasma contamination. The Asian lineage ZIKV SZ01 strain (GenBank accession no. KU866423) was amplified in C6/36 cells. Virus stocks were titrated by standard plaque assays on Vero cells (55).

Formation of Neurospheres. Neurospheres were generated as previously described (21). Briefly, hNPCs were cultured until 80% confluence and split with Accutase (EMD Millipore). Cells were resuspended and maintained in ReNcell Maintenance Medium, and grown with rotation at 90 rpm for 5 to 7 d.

In Vitro Infection. hNPCs were seeded in six-well plates at 1×10^5 cells per well. At 24 h after seeding, the cells were washed once with PBS and then incubated with ZIKV at the indicated MOI for 2 h at 37 °C. Next, the inoculum was removed and cells were washed once with PBS, and then replaced with fresh medium. Mock-infected cells were incubated with the culture supernatant from uninfected C6/36 cells. The cells were then incubated with ZIKV in the presence of VX-765 for 1 h at 37 °C, washed once with PBS, and cultured with fresh medium. For neurosphere infection, hNPCs were infected with ZIKV at the indicated MOI before the cells were grown with rotation at 90 rpm to form neurospheres.

Mice. WT, *Casp1*$^{-/-}$, and *Ifnar1*$^{-/-}$ mice with C57BL/6 background were bred in pathogen-free animal facilities of Sun Yat-Sen University (SYSU). All animal studies were approved by the SYSU Institutional Animal Care and Use Committee (SYSU IACUC) under protocol no. SYSU-IACUC-2019-B547, and all animal experiments were performed in accordance with the guidelines approved by SYSU IACUC and conducted in a biological safety protection laboratory.

In Vivo Murine Infection. Neonatal mice were infected subcutaneously according to a previously described method (45). Briefly, 5×10^5 PFUs of ZIKV in a volume of 50 μL or the same volume of mock medium was injected subcutaneously into 3-d-old mouse pups of *Casp1*$^{-/-}$ mice or immunocompetent pups. Pups were monitored daily for mortality, and body weight was measured every 3 d from the day of infection until 21 dpi. Mice were humanely killed at 21 dpi or when there was a ≥20% weight loss.

To evaluate the effect of VX-765 and Z-DEVD-FMK on neuropathological outcomes, pups infected with 1×10^6 PFUs of ZIKV received, every 2 d, intraperitoneal injection of VX-765 (50 mg/kg) (Invivogen) or Z-DEVD-FMK (50 mg/kg; MedChemExpress) diluted in PBS/DMSO from 1 dpi until 30 dpi. Vehicle-treated animals received injections of PBS/DMSO every 2 d. Mice were humanely killed at 30 dpi or when there was a ≥20% weight loss.

Ifnar1$^{-/-}$ mice were infected intraperitoneally as previous described (55). Briefly, 5-wk-old *Ifnar1*$^{-/-}$ mice were injected intraperitoneally with 1×10^5 PFUs of ZIKV in a volume of 50 μL or the same volume of mock medium. To determine the effect of VX-765 on neuropathological outcomes, *Ifnar1*$^{-/-}$ mice infected with ZIKV received daily intraperitoneal injections of VX-765 (50 mg/kg) diluted in PBS/DMSO from 1 dpi until the experimental endpoint. Control vehicle-treated animals received daily injections of PBS/DMSO. Mice were evaluated daily for mortality and body weight was measured every 3 d starting from the day of infection. Mice were humanely killed at 15 dpi or when there was a ≥20% weight loss.

Histological Analysis. Mouse brain tissue was harvested and fixed in 4% paraformaldehyde (PFA) for 24 h at room temperature. The fixed tissues were dehydrated overnight, paraffin-embedded, sectioned, rehydrated, and stained with H&E. The H&E-stained sections were analyzed for virus-induced neuropathological damages. Images were obtained using a Zeiss Axio Imager Z2 microscope and analyzed with the ZEN software (Carl Zeiss MicroImaging).

Immunofluorescence. Cultured cells and neurospheres were fixed using 4% PFA in PBS for 15 min at room temperature. All brain tissue sections, cultured cells or neurospheres were permeabilized with 0.2% Triton X-100 and blocked for 1 h at room temperature with 5% BSA in PBS, followed by incubation with the indicated primary antibody overnight at 4 °C. The primary antibodies used were anti-SOX2 (Proteintech Group) and anti-ZIKV Envelope (BioFront Technologies). Alexa Flour 488 or Alexa Flour 555 dye-conjugated secondary antibodies (Life Technologies) and DAPI (Sigma-Aldrich) nuclear counterstaining were used for visualization. Activation of caspase-1 was measured using the FAM-FLICA Caspase-1 Assay Kit (ImmunoChemistry Technologies) according to the manufacturers' instructions. Multiplex immunofluorescence staining was performed using PANO 4-plex IHC Kit (Panovue) according to the manufacturer's suggested protocols. Antibodies used were:

anti-SOX2 (Proteintech Group), anti-ZIKV NS3 (GeneTex), anti–Iba-1 (Wako), anti-GFAP (Abcam), and anticaspase-1 p10 (Thermo Fisher Scientific). DAPI were used as a nuclear counterstain. Images were obtained using a Zeiss LSM880 confocal microscope (Carl Zeiss MicroImaging). The manual counting of the cells was performed using the built-in cell-counter plugin of the ImageJ program.

IHC. Tissue sections from mouse brain were placed on silane-coated slides, deparaffinized, and hydrated using decreasing concentrations of ethanol. Sections were then incubated with 3% hydrogen peroxide (H_2O_2) in methanol for inactivation of endogenous peroxidase, followed by treatment with 0.01 M citrate buffer for 40 min at 95 °C to reactivate the antigens. Subsequently, sections were washed in PBS and incubated with primary antibodies including anti–Iba-1 (Wako) and anti-GFAP (Abcam) overnight at 4 °C. After washing with PBS, sections were incubated with rabbit or mouse biotinylated secondary antibodies (Vector Laboratories) for 1 h at room temperature. Finally, immunoreaction was visualized using streptavidin-biotin-peroxidase with DAB as substrate. Sections were viewed using a Zeiss Axio Imager Z2 microscope (Carl Zeiss MicroImaging).

TEM. Cell pellet was fixed in 2.5% glutaraldehyde (vol/vol) in 100 mM phosphate buffer with 2% PFA (wt/vol) at 4 °C overnight. The next day, postfixation was carried out with 1% of osmium tetroxide in 100 mM phosphate buffer for 1.5 h at room temperature. The cell pellet was then washed, dehydrated in a progressed series of ethanol (50%, 70%, 80%, 90%, and 100%), cleared in acetone, and embedded in Eponate 12 resin (Ted Pella). Ultrathin sections were cut to 60-nm thickness, and stained with 2.0% uranyl acetate solution and 2.0% lead citrate solution. The cells were visualized with the Tecnai G2 Spirit Twin TEM (FEI).

Pyroptosis Assay. Cell pyroptosis was measured as described previously (56). Briefly, hNPCs were seeded in 12-well plates for 24 h, followed by infection with ZIKV or mock control. Thirty-six hours postchallenge, the cells were stained with staining solution containing PI (2 μg/mL) and Hoechst 33342 (5 μg/mL). Dead cells (PI permeable) were determined under a Zeiss Axio Observer Z1 microscope and analyzed with ZEN software (Carl Zeiss MicroImaging) and ImageJ program.

LDH Release Assay. LDH released into cell culture supernatants after distinct treatments was measured using the Lactate Dehydrogenase Assay Kit (Abcam) according to the manufacturer's suggested protocols. Briefly, hNPCs were seeded in 24-well plates for 24 h. The next day the cells were infected with ZIKV or mock infection for 36 h, and supernatants and cell lysates were harvested. The LDH activity in the culture supernatant was expressed as a percentage of total LDH in the cell lysate.

ELISA. Cytokine levels were measured by ELISA using mouse IL-1β and IL-18 ELISA kits (eBiosciences) according to the manufacturer's instructions.

Immunoblotting. The protein extracts were prepared by lysing cells or homogenizing tissues with RIPA lysis buffer (Millipore) containing a mixture of protease and phosphatase inhibitors (Sigma-Aldrich). Proteins were then separated by PAGE and transferred onto a polyvinylidene difluoride membrane. The membranes were probed with the following primary antibodies: anticaspase-1 (Santa Cruz Biotechnology), anti-human GSDMD (Abcam), anti-mouse GSDMD (Abcam), anti-ZIKV Envelope (BioFront Technologies), anti–β-actin (Proteintech Group). The blotted membranes were incubated with horseradish peroxidase-conjugated secondary antibodies, and the botted signals were visualized by enhanced chemiluminescence with a commercially available detection kit (Thermo Fisher Scientific) according to the manufacturer's suggested protocols.

qRT-PCR. Total RNA was extracted from mouse brain tissues with TRIzol (Invitrogen) according to the manufacturer's instructions. First-strand cDNA synthesis was performed using random hexamer primers, and qRT-PCR was carried out by using the ChamQ SYBR qPCR Master Mix (Vazyme). All readings were normalized to the level of hypoxanthine phosphoribosyltransferase mRNA. Viral RNA was detected and quantitated as previously described (20).

Statistical Analyses. The results are expressed as mean values (±SDs). Statistical analyses were performed on triplicate experiments, using a two-tailed

1. G. W. Dick, Zika virus. II. Pathogenicity and physical properties. *Trans. R. Soc. Trop. Med. Hyg.* **46**, 521–534 (1952).
2. D. Musso *et al.*, Potential sexual transmission of Zika virus. *Emerg. Infect. Dis.* **21**, 359–361 (2015).
3. World Health Organization, Zika epidemiology update. https://www.who.int/emergencies/diseases/zika/epidemiology-update/en/. Accessed 2 July 2019.
4. J. Cerbino-Neto *et al.*, Clinical manifestations of Zika virus infection, Rio de Janeiro, Brazil, 2015. *Emerg. Infect. Dis.* **22**, 1318–1320 (2016).
5. J. Mlakar *et al.*, Zika virus associated with microcephaly. *N. Engl. J. Med.* **374**, 951–958 (2016).
6. S. A. Rasmussen, D. J. Jamieson, M. A. Honein, L. R. Petersen, Zika virus and birth defects—Reviewing the evidence for causality. *N. Engl. J. Med.* **374**, 1981–1987 (2016).
7. T. Dos Santos *et al.*, Zika virus and the Guillain-Barré syndrome—Case series from seven countries. *N. Engl. J. Med.* **375**, 1598–1601 (2016).
8. C. N. Soares *et al.*, Fatal encephalitis associated with Zika virus infection in an adult. *J. Clin. Virol.* **83**, 63–65 (2016).
9. G. Carteaux *et al.*, Zika virus associated with meningoencephalitis. *N. Engl. J. Med.* **374**, 1595–1596 (2016).
10. O. J. Brady *et al.*, The association between Zika virus infection and microcephaly in Brazil 2015-2017: An observational analysis of over 4 million births. *PLoS Med.* **16**, e1002755 (2019).
11. World Health Organization, Zika situation report. https://www.who.int/emergencies/zika-virus/situation-report/10-march-2017/en/. Accessed 10 March 2017.
12. A. S. Melo *et al.*, Congenital Zika virus infection: Beyond neonatal microcephaly. *JAMA Neurol.* **73**, 1407–1416 (2016).
13. C. A. Moore *et al.*, Characterizing the pattern of anomalies in congenital Zika syndrome for pediatric clinicians. *JAMA Pediatr.* **171**, 288–295 (2017).
14. W. K. de Oliveira *et al.*, Zika virus infection and associated neurologic disorders in Brazil. *N. Engl. J. Med.* **376**, 1591–1593 (2017).
15. M. Sarno *et al.*, Zika virus infection and stillbirths: A case of hydrops fetalis, hydranencephaly and fetal demise. *PLoS Negl. Trop. Dis.* **10**, e0004517 (2016).
16. G. Calvet *et al.*, Detection and sequencing of Zika virus from amniotic fluid of fetuses with microcephaly in Brazil: A case study. *Lancet Infect. Dis.* **16**, 653–660 (2016).
17. R. B. Martines *et al.*, Notes from the field: Evidence of Zika virus infection in brain and placental tissues from two congenitally infected newborns and two fetal losses—Brazil, 2015. *MMWR Morb. Mortal. Wkly. Rep.* **65**, 159–160 (2016).
18. C. Li *et al.*, Zika virus disrupts neural progenitor development and leads to microcephaly in mice. *Cell Stem Cell* **19**, 120–126 (2016).
19. H. Li *et al.*, Zika virus infects neural progenitors in the adult mouse brain and alters proliferation. *Cell Stem Cell* **19**, 593–598 (2016).
20. F. R. Cugola *et al.*, The Brazilian Zika virus strain causes birth defects in experimental models. *Nature* **534**, 267–271 (2016).
21. P. P. Garcez *et al.*, Zika virus impairs growth in human neurospheres and brain organoids. *Science* **352**, 816–818 (2016).
22. Z. Wen, H. Song, G. L. Ming, How does Zika virus cause microcephaly? *Genes Dev.* **31**, 849–861 (2017).
23. B. T. Cookson, M. A. Brennan, Pro-inflammatory programmed cell death. *Trends Microbiol.* **9**, 113–114 (2001).
24. R. B. Martines *et al.*, Pathology of congenital Zika syndrome in Brazil: A case series. *Lancet* **388**, 898–904 (2016).
25. J. R. de Sousa *et al.*, In situ inflammasome activation results in severe damage to the central nervous system in fatal Zika virus microcephaly cases. *Cytokine* **111**, 255–264 (2018).
26. Z. He *et al.*, NLRP3 inflammasome activation mediates Zika virus-associated inflammation. *J. Infect. Dis.* **217**, 1942–1951 (2018).
27. W. Wang *et al.*, Zika virus infection induces host inflammatory responses by facilitating NLRP3 inflammasome assembly and interleukin-1β secretion. *Nat. Commun.* **9**, 106 (2018).
28. J. Shi, W. Gao, F. Shao, Pyroptosis: Gasdermin-mediated programmed necrotic cell death. *Trends Biochem. Sci.* **42**, 245–254 (2017).
29. F. Martinon, K. Burns, J. Tschopp, The inflammasome: A molecular platform triggering activation of inflammatory caspases and processing of proIL-beta. *Mol. Cell* **10**, 417–426 (2002).
30. S. L. Fink, B. T. Cookson, Caspase-1-dependent pore formation during pyroptosis leads to osmotic lysis of infected host macrophages. *Cell. Microbiol.* **8**, 1812–1825 (2006).
31. W. T. He *et al.*, Gasdermin D is an executor of pyroptosis and required for interleukin-1β secretion. *Cell Res.* **25**, 1285–1298 (2015).
32. X. Liu *et al.*, Inflammasome-activated gasdermin D causes pyroptosis by forming membrane pores. *Nature* **535**, 153–158 (2016).
33. J. Ding *et al.*, Pore-forming activity and structural autoinhibition of the gasdermin family. *Nature* **535**, 111–116 (2016).
34. T. Strowig, J. Henao-Mejia, E. Elinav, R. Flavell, Inflammasomes in health and disease. *Nature* **481**, 278–286 (2012).
35. M. Kovarova *et al.*, NLRP1-dependent pyroptosis leads to acute lung injury and morbidity in mice. *J. Immunol.* **189**, 2006–2016 (2012).
36. S. L. Masters *et al.*, NLRP1 inflammasome activation induces pyroptosis of hematopoietic progenitor cells. *Immunity* **37**, 1009–1023 (2012).
37. G. Doitsh *et al.*, Cell death by pyroptosis drives CD4 T-cell depletion in HIV-1 infection. *Nature* **505**, 509–514 (2014).
38. B. D. Semple, K. Blomgren, K. Gimlin, D. M. Ferriero, L. J. Noble-Haeusslein, Brain development in rodents and humans: Identifying benchmarks of maturation and vulnerability to injury across species. *Prog. Neurobiol.* **106-107**, 1–16 (2013).
39. B. Clancy, R. B. Darlington, B. L. Finlay, Translating developmental time across mammalian species. *Neuroscience* **105**, 7–17 (2001).
40. S. Mariathasan *et al.*, Cryopyrin activates the inflammasome in response to toxins and ATP. *Nature* **440**, 228–232 (2006).
41. F. Bassil *et al.*, Reducing C-terminal truncation mitigates synucleinopathy and neurodegeneration in a transgenic model of multiple system atrophy. *Proc. Natl. Acad. Sci. U.S.A.* **113**, 9593–9598 (2016).
42. J. Flores *et al.*, Caspase-1 inhibition alleviates cognitive impairment and neuropathology in an Alzheimer's disease mouse model. *Nat. Commun.* **9**, 3916 (2018).
43. E. C. Gilmore, C. A. Walsh, Genetic causes of microcephaly and lessons for neuronal development. *Wiley Interdisc. Rev. Dev. Biol.* **2**, 461–478 (2013).
44. World Health Organization, Microcephaly. https://www.who.int/news-room/fact-sheets/detail/microcephaly. Accessed 16 February 2018.
45. I. Nem de Oliveira Souza *et al.*, Acute and chronic neurological consequences of early-life Zika virus infection in mice. *Sci. Transl. Med.* **10**, eaar2749 (2018).
46. A. N. van den Pol, G. Mao, Y. Yang, S. Ornaghi, J. N. Davis, Zika virus targeting in the developing brain. *J. Neurosci.* **37**, 2161–2175 (2017).
47. A. Baroja-Mazo *et al.*, The NLRP3 inflammasome is released as a particulate danger signal that amplifies the inflammatory response. *Nat. Immunol.* **15**, 738–748 (2014).
48. W. Wannamaker *et al.*, (S)-1-((S)-2-{[1-(4-amino-3-chloro-phenyl)-methanoyl]-amino}-3,3-dimethyl-butanoy l)-pyrrolidine-2-carboxylic acid ((2R,3S)-2-ethoxy-5-oxo-tetrahydro-furan-3-yl)-amide (VX-765), an orally available selective interleukin (IL)-converting enzyme/caspase-1 inhibitor, exhibits potent anti-inflammatory activities by inhibiting the release of IL-1beta and IL-18. *J. Pharmacol. Exp. Ther.* **321**, 509–516 (2007).
49. M. Bialer *et al.*, Progress report on new antiepileptic drugs: A summary of the Eleventh Eilat Conference (EILAT XI). *Epilepsy Res.* **103**, 2–30 (2013).
50. N. Gomez-Lopez *et al.*, A role for the inflammasome in spontaneous labor at term with acute histologic chorioamnionitis. *Reprod. Sci.* **24**, 934–953 (2017).
51. J. W. Upton, F. K. Chan, Staying alive: Cell death in antiviral immunity. *Mol. Cell* **54**, 273–280 (2014).
52. A. Skaletskaya *et al.*, A cytomegalovirus-encoded inhibitor of apoptosis that suppresses caspase-8 activation. *Proc. Natl. Acad. Sci. U.S.A.* **98**, 7829–7834 (2001).
53. O. P. Zhirnov, T. E. Konakova, T. Wolff, H. D. Klenk, NS1 protein of influenza A virus down-regulates apoptosis. *J. Virol.* **76**, 1617–1625 (2002).
54. S. H. Choi *et al.*, A three-dimensional human neural cell culture model of Alzheimer's disease. *Nature* **515**, 274–278 (2014).
55. M. T. Aliota *et al.*, Characterization of lethal Zika virus infection in AG129 mice. *PLoS Negl. Trop. Dis.* **10**, e0004682 (2016).
56. Q. B. Zha *et al.*, ATP-induced inflammasome activation and pyroptosis is regulated by AMP-activated protein kinase in macrophages. *Front. Immunol.* **7**, 597 (2016).